



Cite this: *Chem. Commun.*, 2020, **56**, 619

Received 22nd September 2019,  
Accepted 6th December 2019

DOI: 10.1039/c9cc07447c

[rsc.li/chemcomm](http://rsc.li/chemcomm)

## A highly $\text{Li}^+$ -conductive $\text{HfNb}_{24}\text{O}_{62}$ anode material for superior $\text{Li}^+$ storage<sup>†</sup>

Qingfeng Fu,<sup>ab</sup> Haijie Cao,<sup>a</sup> Guisheng Liang,<sup>b</sup> Lijie Luo,<sup>b</sup> Yongjun Chen,<sup>b</sup> Vignesh Murugadoss,<sup>cd</sup> Shide Wu,<sup>cf</sup> Tao Ding,<sup>g</sup> Chunfu Lin<sup>g</sup> <sup>\*ab</sup> and Zhanhu Guo <sup>\*c</sup>

**Highly  $\text{Li}^+$ -conductive  $\text{HfNb}_{24}\text{O}_{62}$  is explored as a new intercalation-type niobium-based oxide anode material for superior  $\text{Li}^+$  storage.  $\text{HfNb}_{24}\text{O}_{62}$  owns a Wadsley–Roth shear structure with a large unit-cell volume, leading to a large  $\text{Li}^+$  diffusion coefficient.  $\text{HfNb}_{24}\text{O}_{62}$  shows a large capacity, safe operating potential, high rate performance and good cyclability.**

Safe lithium-ion batteries (LIBs) with high power and energy density for electric vehicles (EVs) and hybrid electric vehicles (HEVs) have attracted intense attention.<sup>1</sup> However, the traditional graphite anode material is limited in such applications due to its low kinetics and unsafe lithiation potential.<sup>2</sup> As a promising substitute for graphite,  $\text{Li}_4\text{Ti}_5\text{O}_{12}$  is appealing due to its safe operating potential ( $\sim 1.57$  V) and high rate performance after proper modifications.<sup>3</sup> However, the small theoretical capacity of  $\text{Li}_4\text{Ti}_5\text{O}_{12}$  ( $175 \text{ mA h g}^{-1}$ ) has limited its large-scale applications. Therefore, new anode materials for safe, high-power and high-energy LIBs have been pursued.

In recent years, intercalation-type niobium-based oxides, such as  $\text{Ti}_2\text{Nb}_{2x}\text{O}_{4+5x}$  ( $x = 2, 5$  and  $24$ ),<sup>4–11</sup>  $\text{MNb}_{11}\text{O}_{29}$  ( $\text{M} = \text{Al, Cr, Fe and Ga}$ ),<sup>12–15</sup> and  $\text{W}_5\text{Nb}_{16}\text{O}_{55}$ ,<sup>16</sup> have been developed as potential candidates to replace  $\text{Li}_4\text{Ti}_5\text{O}_{12}$  due to their comparably safe operating

potentials and much larger theoretical/practical capacities. Niobium is an appealing redox center in electrode materials because of its safe potential window in the range of 1.0–2.0 V for the redox couples of  $\text{Nb}^{4+}/\text{Nb}^{5+}$  and  $\text{Nb}^{3+}/\text{Nb}^{4+}$ , which can avoid the formation of dangerous lithium dendrites.<sup>4</sup> In light of multivalent properties, niobium-based oxides can deliver large theoretical capacities of 374–416  $\text{mA h g}^{-1}$ , which are close to that of graphite and significantly surpass that of  $\text{Li}_4\text{Ti}_5\text{O}_{12}$ . In addition, with reported open Wadsley–Roth shear crystal structures consisting of 96–100%  $\text{MO}_6$  octahedra and 0–4%  $\text{MO}_4$  tetrahedra,<sup>4</sup> niobium-based oxides have been identified as typical intercalation-pseudocapacitive materials, which are beneficial for the capacity and fast-charging property. Despite such attractive features, niobium-based oxide anodes still show poor rate performance due to their intrinsically low  $\text{Li}^+$  conductivities. Therefore, developing new niobium-based oxide anode materials with high  $\text{Li}^+$  conductivities,  $\text{Li}^+$ -storage capacities, rate performance, and long-term stability is essential.

In this study,  $\text{HfNb}_{24}\text{O}_{62}$  was synthesized by a facile and cost-effective solid-state reaction, and applied as a novel niobium-based oxide anode material with a high  $\text{Li}^+$  conductivity to boost the  $\text{Li}^+$  storage. In octahedral coordination, the  $\text{Hf}^{4+}$  ionic radius (0.710 Å) is larger than those of  $\text{Ti}^{4+}$  (0.605 Å),  $\text{Al}^{3+}$  (0.535 Å),  $\text{Cr}^{3+}$  (0.615 Å),  $\text{Fe}^{3+}$  (0.550 Å),  $\text{Ga}^{3+}$  (0.620 Å) and  $\text{W}^{6+}$  (0.600),<sup>17</sup> leading to increased lattice constants and unit-cell volume in  $\text{HfNb}_{24}\text{O}_{62}$ . A larger unit-cell volume usually corresponds to faster  $\text{Li}^+$  diffusivity, benefiting the  $\text{Li}^+$  transport kinetics.<sup>18</sup> Moreover,  $\text{HfNb}_{24}\text{O}_{62}$  exhibits a monoclinic Wadsley–Roth shear crystal structure (space group of  $C2$ ) consisting of 96% edge-sharing  $(\text{Hf},\text{Nb})\text{O}_6$  octahedra linked by 4%  $(\text{Hf},\text{Nb})\text{O}_4$  tetrahedra, in which  $\text{Hf}^{4+}$  and  $\text{Nb}^{5+}$  are disorder located. This three-dimensional skeleton bestows fast  $\text{Li}^+$  diffusivity and high structural stability, guaranteeing fast lithiation/delithiation and excellent cyclability. Both the  $\text{HfNb}_{24}\text{O}_{62}/\text{Li}$  half-cell and  $\text{LiNi}_{0.5}\text{Mn}_{1.5}\text{O}_4/\text{HfNb}_{24}\text{O}_{62}$  full-cell exhibit superior electrochemical properties for fast-charging, large-capacity, safe and durable  $\text{Li}^+$  storage.

The detailed crystal structure of the as-prepared  $\text{HfNb}_{24}\text{O}_{62}$  material was studied by XRD and a Rietveld refinement of the XRD pattern (Fig. 1a).<sup>19</sup> The characteristic peaks of  $\text{HfNb}_{24}\text{O}_{62}$

<sup>a</sup> Institute of Materials for Energy and Environment, School of Materials Science and Engineering, Qingdao University, Qingdao 266071, China.

E-mail: [linchunfu@qdu.edu.cn](mailto:linchunfu@qdu.edu.cn)

<sup>b</sup> School of Materials Science and Engineering, Hainan University, Haikou 570228, China

<sup>c</sup> Integrated Composites Laboratory (ICL), Department of Chemical and Biomolecular Engineering, University of Tennessee, Knoxville, TN 37996, USA.

E-mail: [zguo10@utk.edu](mailto:zguo10@utk.edu)

<sup>d</sup> Key Laboratory of Materials Processing and Mold (Zhengzhou University), Ministry of Education, National Engineering Research Center for Advanced Polymer Processing Technology, Zhengzhou University, Zhengzhou 450002, China

<sup>e</sup> College of Chemical and Environmental Engineering, Shandong University of Science and Technology, Qingdao 266590, China

<sup>f</sup> Henan Provincial Key Laboratory of Surface and Interface Science, Zhengzhou University of Light Industry, Zhengzhou 450001, China

<sup>g</sup> College of Chemistry and Chemical Engineering, Henan University, Kaifeng 475004, China

<sup>†</sup> Electronic supplementary information (ESI) available. See DOI: [10.1039/c9cc07447c](https://doi.org/10.1039/c9cc07447c)

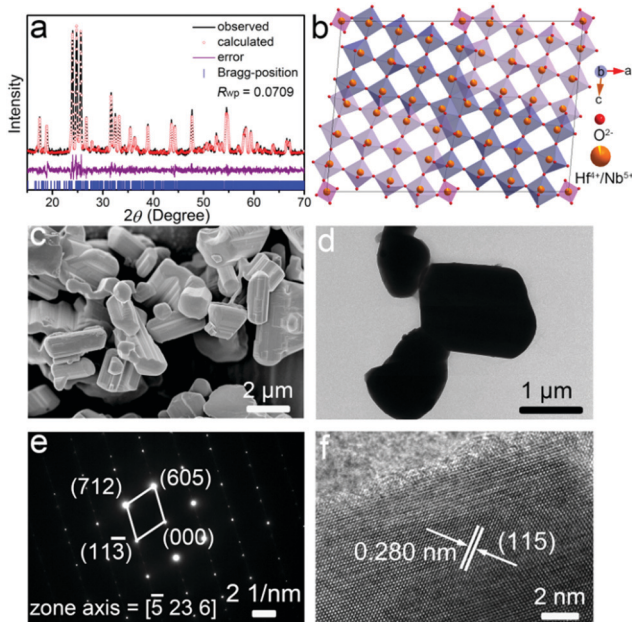


Fig. 1 (a) XRD pattern, (b) crystal structure, (c) FESEM image, (d) TEM image, (e) SAED pattern, and (f) HRTEM image of  $\text{HfNb}_{24}\text{O}_{62}$ .  $R_{wp}$ : weighted profile residual.

are consistent with those of  $\text{TiNb}_{24}\text{O}_{62}$  (space group of  $C2$ ).<sup>6</sup>  $\text{HfNb}_{24}\text{O}_{62}$  owns a robust crystal structure, with the structural unit having a  $3 \times 4$   $(\text{Hf}, \text{Nb})\text{O}_6$  octahedron-block and a half  $(\text{Hf}, \text{Nb})\text{O}_4$  tetrahedron at the block corner (Fig. 1b). The lattice parameters were Rietveld-refined to be  $a = 29.92508(125)$  Å,  $b = 3.82525(14)$  Å,  $c = 21.21133(87)$  Å,  $\beta = 95.068(5)$ °, and  $V = 2418.588(167)$  Å<sup>3</sup>. Detailed lattice parameters are given in Table S1 (ESI†). Due to the larger  $\text{Hf}^{4+}$  (0.710 Å) ionic radius than  $\text{Ti}^{4+}$  (0.605 Å), the unit-cell volume of  $\text{HfNb}_{24}\text{O}_{62}$  is larger than that of  $\text{TiNb}_{24}\text{O}_{62}$ ,<sup>6</sup> which implies wider  $\text{Li}^+$  transport pathways in the  $\text{HfNb}_{24}\text{O}_{62}$  lattice. The survey XPS spectrum of  $\text{HfNb}_{24}\text{O}_{62}$  reveals the presence of Hf, Nb, O and C (reference) elements (Fig. S1a, ESI†). The detailed Hf-4f (Fig. S1b, ESI†) and Nb-3d (Fig. S1c, ESI†) spectra indicate that the Hf and Nb valence states are +4 and +5,<sup>4,20</sup> respectively.

The FESEM (Fig. 1c) and TEM (Fig. 1d) images reveal that the  $\text{HfNb}_{24}\text{O}_{62}$  material is composed of irregular and dense particles with particle sizes varying from  $\sim 2$  to  $\sim 10$  μm, giving a low specific surface area of  $0.38 \text{ m}^2 \text{ g}^{-1}$  (Fig. S2, ESI†). The corresponding SAED pattern in Fig. 1e confirms high crystallinity and reveals a single-crystalline feature of the  $\text{HfNb}_{24}\text{O}_{62}$  primary particles. An interplanar spacing of 0.280 nm measured from the HRTEM image (Fig. 1f) corresponds to the (115) crystallographic plane of  $\text{HfNb}_{24}\text{O}_{62}$ . Besides, the EDX mappings (Fig. S3, ESI†) indicate that the Nb, O and Hf elements are well-dispersed in the whole microparticle, verifying the formation of pure  $\text{HfNb}_{24}\text{O}_{62}$ .

The electrochemical properties of  $\text{HfNb}_{24}\text{O}_{62}$  were mainly studied using half-cells. Fig. 2a shows the CV curves of the  $\text{HfNb}_{24}\text{O}_{62}/\text{Li}$  cell for the initial four cycles at a sweep rate of  $0.2 \text{ mV s}^{-1}$ . The difference in the discharge portion of the first CV curve from the subsequent cycles is likely due to the

incomplete  $\text{Li}^+$  extraction from the  $\text{HfNb}_{24}\text{O}_{62}$  lattice in the first cycle.<sup>21</sup> After the first cycle, the peak positions and corresponding currents are very stable, suggesting good electrochemical reversibility and cyclability of  $\text{HfNb}_{24}\text{O}_{62}$ . In the subsequent sweeps, two highly overlapping CV peak pairs located at  $\sim 2.0/\sim 2.0$  and  $1.77/1.55$  V were assigned to the reversible transformation for the redox couple of  $\text{Nb}^{4+}/\text{Nb}^{5+}$ . The shoulder peaks located at  $1.34/1.14$  V correspond to the redox couple of  $\text{Nb}^{3+}/\text{Nb}^{4+}$ .<sup>12</sup> Consequently, the estimated  $\text{HfNb}_{24}\text{O}_{62}$  mean operating potential ( $\sim 1.66$  V) based on the intermediate potential of two intensive peaks at  $1.77/1.55$  V is close to those of  $\text{Li}_4\text{Ti}_5\text{O}_{12}$  ( $\sim 1.57$  V),<sup>3</sup>  $\text{TiNb}_2\text{O}_7$  ( $\sim 1.64$  V),<sup>5</sup>  $\text{TiNb}_{24}\text{O}_{62}$  ( $\sim 1.66$  V)<sup>6</sup> and  $\text{Ti}_2\text{Nb}_{10}\text{O}_{29}$  ( $\sim 1.70$  V).<sup>11</sup> Such a reasonably high operating potential of  $\text{HfNb}_{24}\text{O}_{62}$  indicates its high safety performance.

Fig. 2b displays the initial three-cycle discharging/charging curves of the  $\text{HfNb}_{24}\text{O}_{62}/\text{Li}$  cell recorded at 0.1C. The observed typical potential plateau at  $\sim 1.66$  V in the discharging/charging curves resulted from a double-phase transformation reaction. The sloping regions at  $3.0$ – $1.67$  and  $1.65$ – $0.8$  V were assigned to two different solid–solution reactions.<sup>8</sup>  $\text{HfNb}_{24}\text{O}_{62}$  shows an initial Coulombic efficiency of 93.8% and large reversible capacity of  $272 \text{ mA h g}^{-1}$  at 0.1C. This practical capacity of  $\text{HfNb}_{24}\text{O}_{62}$  is  $>100 \text{ mA h g}^{-1}$  larger than that of  $\text{Li}_4\text{Ti}_5\text{O}_{12}$  and surpasses the majority of the reported intercalation-type niobium-based oxide anode materials (Fig. 2c).<sup>3,4,6,9,10,14–16,22,23</sup> The high initial Coulombic efficiency can be due to the fact that little SEI layers formed on the  $\text{HfNb}_{24}\text{O}_{62}$  particle surfaces above 0.8 V.

The rate performance of  $\text{HfNb}_{24}\text{O}_{62}$  was investigated at various current rates for every ten cycles, as shown in Fig. 2d and e.  $\text{HfNb}_{24}\text{O}_{62}$  delivers large reversible capacities of 223, 195, 174, 138 and  $105 \text{ mA h g}^{-1}$  at 0.5, 1, 2, 5 and 10C, respectively. When the current rate gradually returns from 10C to 0.5C, the capacity is recovered to its original value. When cycled at 1C,  $\text{HfNb}_{24}\text{O}_{62}$  shows a small capacity change from 193 to  $182 \text{ mA h g}^{-1}$  after 100 cycles, giving 94.3% capacity retention (Fig. 2f and Fig. S4, ESI†). When cycled at 10C,  $\text{HfNb}_{24}\text{O}_{62}$  shows 87.1% capacity retention even after 500 cycles during the prolonged cycling (Fig. 2g and Fig. S5, ESI†). Such superior cyclability can be due to the stable crystal structure and good  $\text{Li}^+$ -transport kinetics of  $\text{HfNb}_{24}\text{O}_{62}$ .

To interpret the high rate performance of  $\text{HfNb}_{24}\text{O}_{62}$ , its  $\text{Li}^+$ -storage kinetics was analyzed by additional CV experiments recorded at different sweep rates (Fig. 2h). It was found that the cathodic/anodic CV peak current exhibited power law dependence on the sweep rate with an exponent of 0.67/0.74 (Fig. 2i),<sup>7,24</sup> suggesting that the pseudocapacitive behaviour significantly contributed to the fast charge storage of  $\text{HfNb}_{24}\text{O}_{62}$  since it is well known that exponents of 0.5 and 1 indicate diffusion-controlled and pseudocapacitive charge storage, respectively.

A galvanostatic intermittent titration technique (GITT) with a current pulse at 0.1C for 10 min between rest intervals for 20 min was applied to elucidate the  $\text{Li}^+$  diffusion coefficient ( $D_{\text{Li}}$ ) of  $\text{HfNb}_{24}\text{O}_{62}$  during the initial two cycles. Based on Fick's second law (see ESI†),<sup>25</sup> the evolving  $D_{\text{Li}}$  of  $\text{HfNb}_{24}\text{O}_{62}$  at each potential in the discharging (lithiation) and charging (delithiation) processes is determined and plotted in Fig. 2j. The  $D_{\text{Li}}$  values show

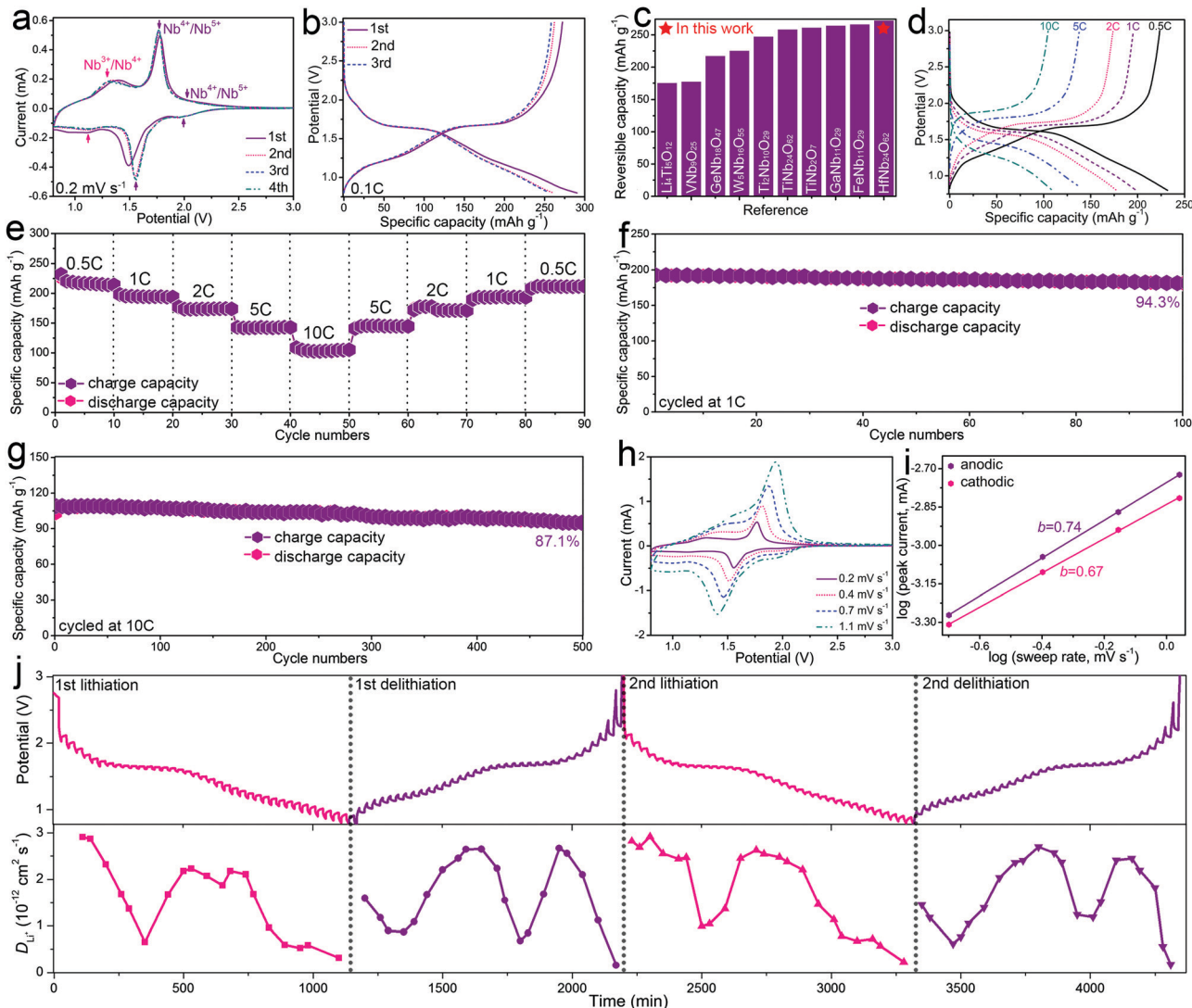


Fig. 2 Electrochemical characterizations of the  $\text{HfNb}_{24}\text{O}_{62}/\text{Li}$  cell: (a) CVs at  $0.2 \text{ mV s}^{-1}$ , (b) discharging/charging curves at  $0.1\text{C}$ , (c) comparisons of reversible capacity of  $\text{HfNb}_{24}\text{O}_{62}$  with other intercalation-type oxide anode materials, (d) discharging/charging curves at different current rates, (e) rate performance, cyclability at (f)  $1\text{C}$  and (g)  $10\text{C}$ , (h) CVs at different sweeping rates, (i) exponential relationship between CV peak current and sweep rate, and (j) GITT curves and corresponding  $\text{Li}^+$  diffusion coefficients (initial two cycles).

a similar variation trend in the two cycles, and minor values appear in the plateau region ( $\sim 1.7 \text{ V}$ ), where the  $\text{Li}^+$  interaction with the host matrix is strong during the two-phase transition reaction. During the first lithiation/delithiation processes, the  $D_{\text{Li}}$  value varies from  $1.51 \times 10^{-13}$  to  $2.91 \times 10^{-12} \text{ cm}^2 \text{ s}^{-1}$ , averaging at  $1.61 \times 10^{-12} \text{ cm}^2 \text{ s}^{-1}$ . The average  $D_{\text{Li}}$  value in the second lithiation/delithiation processes ( $1.70 \times 10^{-12} \text{ cm}^2 \text{ s}^{-1}$ ) is slightly larger than that of the initial cycle, but the curves are similar to those in the initial cycle. It is noteworthy that the  $\text{Li}^+$  diffusion coefficient of  $\text{HfNb}_{24}\text{O}_{62}$  is significantly larger than those of the reported niobium-based oxide anode materials (Table S2, ESI†), which can be ascribed to its open Wadsley-Roth shear crystal structure with an enlarged unit-cell volume. Clearly, the fast  $\text{Li}^+$  diffusivity together with the significant pseudocapacitive behaviour of  $\text{HfNb}_{24}\text{O}_{62}$  greatly contributes to its superior  $\text{Li}^+$  storage (especially its rate performance).

To demonstrate the practical application of  $\text{HfNb}_{24}\text{O}_{62}$ , a full cell with a  $\text{HfNb}_{24}\text{O}_{62}$  anode and a  $\text{LiNi}_{0.5}\text{Mn}_{1.5}\text{O}_4$  cathode was fabricated (Fig. 3a). The  $\text{LiNi}_{0.5}\text{Mn}_{1.5}\text{O}_4/\text{HfNb}_{24}\text{O}_{62}$  full cell affords a large charge capacity of  $213 \text{ mA h g}^{-1}$  with an average operating voltage of  $\sim 3.0 \text{ V}$  at  $0.1\text{C}$  (Fig. 3b). This high voltage agrees with the CV result (Fig. 3c). As the current rate gradually increases to  $0.5, 1, 2, 5$  and even  $10\text{C}$ , the reversible capacity retains  $143, 130, 116, 95$  and  $78 \text{ mA h g}^{-1}$ , respectively (Fig. 3d). When the current rate returns from  $10\text{C}$  to  $0.5\text{C}$ , the obtained capacity of  $141 \text{ mA h g}^{-1}$  indicates good electrochemical reversibility (Fig. 3e). The full cell also presents outstanding cyclability at both  $1\text{C}$  (83.4% capacity retention after 100 cycles, Fig. 3f) and  $5\text{C}$  (84.7% capacity retention after 500 cycles, Fig. 3g). The full cell can power a green light-emitting diode (LED) after being cycled 500 times at  $5\text{C}$  (Fig. 3g inset).

In summary, highly- $\text{Li}^+$ -conductive  $\text{HfNb}_{24}\text{O}_{62}$  is demonstrated as a novel anode material to realize superior  $\text{Li}^+$  storage.

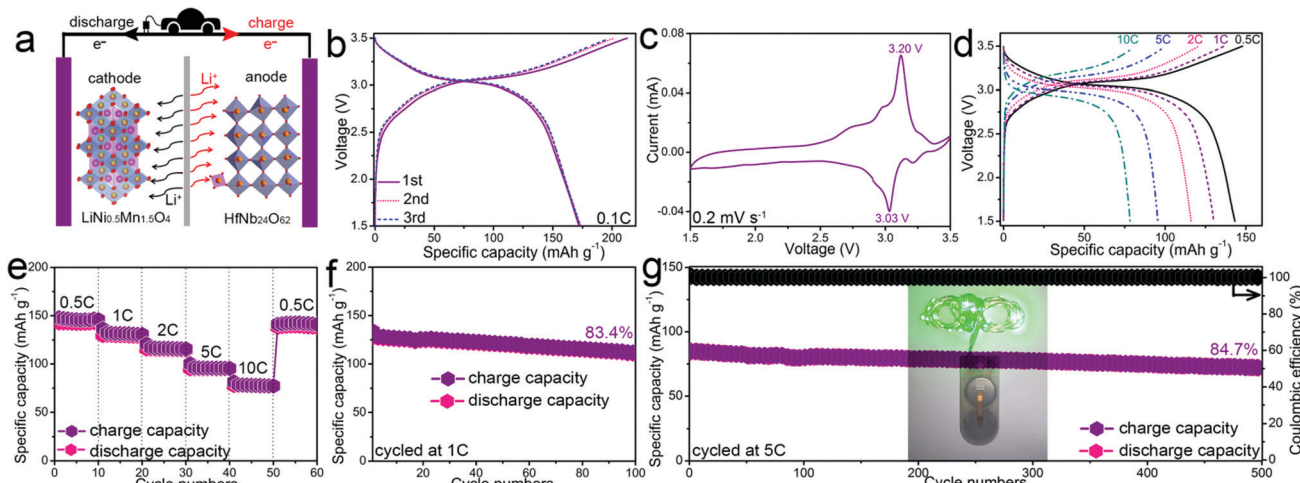


Fig. 3 (a) Schematic illustration of the  $\text{LiNi}_{0.5}\text{Mn}_{1.5}\text{O}_4$ // $\text{HfNb}_{24}\text{O}_{62}$  full cell. Electrochemical characterizations of the  $\text{LiNi}_{0.5}\text{Mn}_{1.5}\text{O}_4$ // $\text{HfNb}_{24}\text{O}_{62}$  full cell: (b) initial three-cycle charging/discharging curves at  $0.1\text{C}$ , (c) CV at  $0.2\text{ mV s}^{-1}$ , (d) charging/discharging curves at different current rates, (e) rate performance, and cyclability at (f)  $1\text{C}$  and (g)  $5\text{C}$  (inset: green LED lit up by the full cell).

Both the open Wadsley–Roth shear crystal structure and enlarged unit-cell volume lead to favorable  $\text{Li}^+$  conduction. Benefiting from the robust host framework and fast ion diffusion pathways,  $\text{HfNb}_{24}\text{O}_{62}$  exhibits prominent electrochemical properties. At  $0.1\text{C}$ , it displays a large capacity of  $272\text{ mA h g}^{-1}$  with a relatively safe operating potential of  $\sim 1.66\text{ V}$  and a high initial Coulombic efficiency of  $93.8\%$ . Even at  $10\text{C}$ , a remarkable reversible capacity of  $105\text{ mA h g}^{-1}$  is preserved. Furthermore, it exhibits good long-term cyclability, as indicated by  $87.1\%$  capacity retention after  $500$  cycles at  $10\text{C}$ . More importantly, a  $\text{LiNi}_{0.5}\text{Mn}_{1.5}\text{O}_4$ // $\text{HfNb}_{24}\text{O}_{62}$  full cell also exhibits high rate performance with  $213\text{ mA h g}^{-1}$  at  $0.1\text{C}$  and  $78\text{ mA h g}^{-1}$  at  $10\text{C}$ , and good long-term cyclability with  $84.7\%$  capacity retention after  $500$  cycles at  $5\text{C}$ . This work can benefit the future designs of highly- $\text{Li}^+$ -conductive and fast-charging electrode materials.

This work was supported by the National Natural Science Foundation of China (51762014) and China Postdoctoral Science Foundation (2019M652316).

## Conflicts of interest

There are no conflicts to declare.

## Notes and references

- (a) H. T. Sun, L. Mei and J. F. Liang, *et al.*, *Science*, 2017, **356**, 599; (b) Y. Zhang, Y. An and L. Wu, *et al.*, *J. Mater. Chem. A*, 2019, **7**, 19668; (c) C. Hou, J. Wang and W. Du, *et al.*, *J. Mater. Chem. A*, 2019, **7**, 13460.
- (a) S. R. Sivakkumar, J. Y. Nerkar and A. G. Pandolfo, *Electrochim. Acta*, 2010, **55**, 3330; (b) M. Idrees, S. Batoool and J. Kong, *et al.*, *Electrochim. Acta*, 2019, **296**, 925; (c) R. Li, C. Lin and N. Wang, *et al.*, *Adv. Compos. Hybrid Mater.*, 2018, **1**, 440.
- (a) C. F. Lin, X. Y. Fan, Y. L. Xin, F. Q. Cheng, M. O. Lai, H. H. Zhou and L. Lu, *J. Mater. Chem. A*, 2014, **2**, 9982; (b) M. Idrees, L. Liu and S. Batoool, *et al.*, *Eng. Sci.*, 2019, **6**, 64.
- L. Hu, L. J. Luo, C. F. Lin, R. J. Li and Y. J. Chen, *J. Mater. Chem. A*, 2018, **6**, 9799.
- C. F. Lin, S. Yu, S. Q. Wu, S. W. Lin, Z. Z. Zhu, J. B. Li and L. Lu, *J. Mater. Chem. A*, 2015, **3**, 8627.
- C. Yang, S. J. Deng, C. F. Lin, S. W. Lin, Y. J. Chen, J. B. Li and H. Wu, *Nanoscale*, 2016, **8**, 18792.
- S. F. Lou, X. Q. Cheng and Y. Zhao, *et al.*, *Nano Energy*, 2017, **34**, 15.
- X. Y. Wu, J. Miao, W. Z. Han, Y. S. Hu, D. F. Chen, J. Lee, J. Kim and L. Q. Chen, *Electrochim. Commun.*, 2012, **25**, 39.
- J. L. Gao, X. Q. Cheng, S. F. Lou, Y. L. Ma, P. J. Zuo, C. Y. Du, Y. Z. Gao and G. P. Yin, *J. Alloys Compd.*, 2017, **728**, 534.
- W. L. Wang, B. Oh, J. Park, H. Ki, J. Jang, G. Lee, H. Hu and M. Ham, *J. Power Sources*, 2015, **300**, 272.
- C. F. Lin, S. Yu, H. Zhao, S. Q. Wu, G. Z. Wang, L. Yu, Y. F. Li, Z. Z. Zhu, J. B. Li and S. W. Lin, *Sci. Rep.*, 2015, **5**, 17836.
- R. T. Zheng, S. S. Qian, X. Cheng, H. X. Yu, N. Peng, T. T. Liu, J. D. Zhang, M. T. Xia, H. J. Zhu and J. Shu, *Nano Energy*, 2019, **58**, 399.
- Q. F. Fu, X. Liu, J. R. Hou, Y. R. Pu, C. F. Lin, L. Yang, X. Z. Zhu, L. Hu, S. W. Lin, L. J. Luo and Y. J. Chen, *J. Power Sources*, 2018, **397**, 231.
- X. M. Lou, C. F. Lin, Q. Luo, J. B. Zhao, B. Wang, J. B. Li, Q. Shao, X. K. Guo, N. Wang and Z. H. Guo, *ChemElectroChem*, 2017, **4**, 3171.
- X. M. Lou, Q. F. Fu, J. Xu, X. Liu, C. F. Lin, J. X. Han, Y. P. Luo, Y. J. Chen, X. Y. Fan and J. B. Li, *ACS Appl. Nano Mater.*, 2018, **1**, 183.
- K. J. Griffith, K. M. Wiaderek, G. Cibin, L. E. Marbella and C. P. Grey, *Nature*, 2018, **559**, 556.
- R. D. Shannon, *Acta Crystallogr., Sect. A: Found. Crystallogr.*, 1976, **32**, 751.
- Y. Wang, W. D. Richards, S. P. Ong, L. J. Miara, J. C. Kim, Y. Mo and G. Ceder, *Nat. Mater.*, 2015, **14**, 1026.
- B. H. Toby, *J. Appl. Crystallogr.*, 2001, **34**, 210.
- A. N. Mansour, *Surf. Sci. Spectra*, 1994, **3**, 221.
- X. Lu, Z. L. Jian, Z. Fang, L. Gu, Y. S. Hu, W. Chen, Z. X. Wang and L. Q. Chen, *Energy Environ. Sci.*, 2011, **4**, 2638.
- F. M. Ran, X. Cheng, H. X. Yu, R. T. Zheng, T. T. Liu, X. F. Li, N. Ren, M. Shui and J. Shu, *Electrochim. Acta*, 2018, **282**, 634.
- G. Li, X. L. Wang and X. M. Ma, *J. Mater. Chem. A*, 2013, **1**, 12409.
- J. P. Yue, C. Suchomski and P. Voepel, *et al.*, *J. Mater. Chem. A*, 2017, **5**, 1978.
- W. Weppner and R. A. Huggins, *J. Electrochem. Soc.*, 1977, **124**, 1569.